Electronic Supplementary Material (ESI) for Dalton Transactions.

Supporting Information

High-sensitivity dual UV/NIR-excited luminescence thermometry by rare earth vanadate nanoparticles

*Rafael V. Perrella and Paulo Cesar de Sousa Filho**

Department of Inorganic Chemistry, Institute of Chemistry, University of Campinas (Unicamp), R. Monteiro Lobato, 270, 13083-970 Campinas, São Paulo, Brazil.

**Corresponding author: pcsfilho@unicamp.br*

Details on luminescence data acquisition and processing

Luminescence spectra were acquired on a Fluorolog 3 (Horiba FL3-22-iHR320) spectrofluorometer equipped with a Hamamatsu R928P photomultiplier detector. Spectra were corrected with relation to the detector sensitivity via the software apparatus. Temperature dependent upconversion and downshift spectra of the particles as powders were obtained between 77 and 673 K using two experimental setups. For temperatures lower than 318 K, the samples were placed in a cryostat (Janis Research Company VNF-100) coupled to the spectrofluorometer. For temperatures higher than 318 K, the samples were put in a platinum crucible in a Linkam Scientific temperature-controlled stage (T95-HT). In this case, the excitation and emission signals were collected by optical fibers (Wavelength Electronics LFI-3751) and guided to the sample and detector, respectively. In both experimental arrangements the samples were thermalized by 10 min (± 0.1 °C) before each signal acquisition. The same power density was set for upconversion measurements (λ_{exc}=980 nm, P=34.8 W cm^{-2}). However, powder density at the sample surface may vary slightly, thermometry calibration curves were fitted for each setup separately. Luminescence spectroscopy of particles as colloids was carried out on quartz cuvettes of 1 cm optical path (3 mL of suspension using PTFE stirrer, 800 rpm), temperatures were set between 288 and 333 K. For downshift measurements the cuvette (5 mmol L^{-1} in $REVO_4$) was placed in a Horiba F-3004 Peltier-controlled sample holder (± 0.1 K). For upconversion detections, the cuvette (50 mmol L^{-1} in $REVO_4$) was put in a FL-1065 sample holder (Horiba) coupled to an external circulating bath (Neslab RTE-111). In this case, the temperature was also monitored by a mercury thermometer (± 0.5 K) placed inside the cuvette to calibrate temperature for laser heating effects, and the pump power was adjusted to 88 W cm^{-2} in order to attain suitable signal to noise ratios. Equilibration steps (10 min) for both powders and colloids were carried out under constant irradiation (λ_{exc} = 980 nm or λ_{exc} = 280 nm). In the case of colloids, averaged spectra of after three acquisitions were considered, and normalized intensities were used for the calculation of intensity ratios because of intensity fluctuations due to decantation/convection/evaporation effects.

For upconversion spectra of particles as powders and colloids, the integrated intensities of the 476 nm (Tm^{3+}, $^1G_4 \rightarrow {}^3H_6$), 525 nm ($Er^{3+}$, $^2H_{11/2} \rightarrow {}^4I_{15/2}$), 553 nm ($Er^{3+}$, $^4S_{3/2} \rightarrow {}^4I_{15/2}$), 658 nm ($Tm^{3+}$, $^1G_4 \rightarrow {}^3F_4$ + Er^{3+}, $^4F_{9/2} \rightarrow {}^4I_{15/2}$) and 700 nm ($Tm^{3+}$, $^3F_{2,3} \rightarrow {}^3H_6$) emissions were obtained from deconvolutions of their respective Stark components using a set of Gaussian functions. This procedure was adopted to separate different contributions in the emission bands that present spectral overlap or to discriminate the

luminescence from the spurious laser signal (overtone). Only the integrated intensity of the Tm^{3+} emission at 801 nm ($^3H_4 \rightarrow {}^3H_6$) was processed by integration between 730 and 830 nm without deconvolution. The intensity of the Er^{3+} ($^2H_{11/2} \rightarrow {}^4I_{15/2}$, 525 nm) and Tm^{3+} ($^3F_{2,3} \rightarrow {}^3H_6$, 700 nm) emissions grew exponentially with temperature, which allowed us to perform temperature dependent ratiometric correlations using the emissions at 476, 553, 658 and 801 nm (namely, I_x/I_{525} and I_x/I_{700}, where x = 476, 553, 658 and 801 nm). For the downshift spectra acquired between 257 and 673 K, the intensity of the Er^{3+} emission at 525 nm showed an exponential growth as a function of temperature without spectral overlap with the VO_4^{3-} emission, allowing to carry out the ratiometric correlations using the other Er^{3+} and Tm^{3+} transitions (i.e., I_x/I_{525}, where x = 476, 553, 658 and 801 nm).

The experimental data concerning the above-mentioned integrated intensity ratios was fitted by an exponential relation (Eq.(S1)):[1,2]

$$\Delta = \left(\frac{I_M}{I_N}\right) = Aexp^{-B/T} \quad \text{(S1)}$$

where, Δ is the thermometric parameter which is defined by the ratio between the integrated intensities of two transitions considered (I_M and I_N), T is the temperature, A is a pre-exponential factor and depends on the multiplicity, radiative decay rates and frequency of the involved transitions and the term B is the Boltzmann-type factor ($\Delta E/k_B$) related to the energy separation between the two emitting levels.

For downshift spectra between 77 and 247 K, the emission of VO_4^{3-} group was correlated with the Tm^{3+} and Er^{3+} emissions. In this case, the intensity ratios involve two transitions belonging to two distinct emitting centres. The classical Mott-Seitz model,[3,4] which considers the competition between radiative and non-radiative transitions of a luminescent centre, was used to rationalize the intensity ratios for this dual-centre-based luminescent system. In order to compare the thermometric correlations performances, two processing approaches were proposed. The first one is based on integrated intensity ratios between Ln^{3+} emissions and VO_4^{3-} emission. Here, the integration intervals were standardized as follows: VO_4^{3-} emission (380-510 nm), $^1G_4 \rightarrow {}^3H_6$ (Tm^{3+}, 462-505 nm), $^2H_{11/2} \rightarrow {}_4I_{15/2}$ (Er^{3+}, 540-600 nm), $^1G_4 \rightarrow {}^3F_4 + {}^4F_{9/2} \rightarrow 4I_{15/2}$ (Tm^{3+} + Er^{3+}, 615-686 nm) and $^3H_4 \rightarrow {}^3H_6$ (Tm^{3+}, 730-830 nm). The data were fitted by a relation described by Eq.(S2):[1,2]

$$\Delta = \left(\frac{I_{Ln^{3+}}}{I_{VO_4^{3-}}}\right) = A * \left[\frac{\left(1 + Bexp^{-C/T}\right)}{\left(1 + Dexp^{-E/T}\right)}\right] \quad \text{(S2)}$$

where, Δ is the thermometric parameter which is defined by the integrated intensity ratio between the Ln^{3+} (Ln^{3+} = Er^{3+} and Tm^{3+}) and VO_4^{3-} emissions ($I_{Ln^{3+}}$ and $I_{VO_4^{3-}}$, respectively). The A, B and D constants stand for the ratios between the non-radiative and radiative probabilities of the deactivation channels of transitions from VO_4^{3-} and Ln^{3+}, and C and E are the activation energies for the thermal quenching process of the respective transitions.

In the second approach, the absolute intensities were taken to perform thermometric correlations instead integrated intensities. This was because the presence of some spectrally overlapped emissions bands. As the thermal quenching effect in VO_4^{3-} emission is more pronounced than in the Tm^{3+} and Er^{3+} emissions (Fig. S14), the mathematical relation that describe the intensity ratio can be describe as (Eq.(3)):[1,2]

$$\Delta = \left(\frac{I_{VO_4^{3-}}}{I_{Ln^{3+}}}\right) = \frac{A}{1 + Bexp^{-C/T}} \quad \text{(S3)}$$

where, Δ is the thermometric parameter defined by the ratio between the absolute intensities of the VO_4^{3-} and Ln^{3+} (Ln^{3+} = Er^{3+} and Tm^{3+}) emissions ($I_{VO_4^{3-}}$ and $I_{Ln^{3+}}$, respectively), A is a constant related to the beam intensity at T=0 K, B is the ratio between the non-radiative and radiative probabilities of the deactivation channels of transitions from VO_4^{3-}, and C is the activation energy for the thermal quenching process.

The errors for each intensity ratio were calculated from fractional uncertainties (δ_F), which were defined as the inverse of the signal-to-noise ratio ($R_{S/N}$, Eq.(S4)):

$$\delta_F = \frac{1}{R_{S/N}} \quad \text{(S4)}$$

The error bars on the integrated intensities (δI_M, δI_N) were taken as the product between fractional uncertainties (δ_F) and integrated intensities (I_M, I_N). For each intensity ratio ($\Delta = I_M/I_N$), the relative error ($\delta\Delta/\Delta$) was calculated as (Eq.(S5)):[1,5]

$$\frac{\delta\Delta}{\Delta} = \sqrt{\left(\frac{\delta I_M}{I_M}\right)^2 + \left(\frac{\delta I_N}{I_N}\right)^2} \quad \text{(S5)}$$

The applicability of the obtained system in luminescent nanothermometry was evaluated from the sensor quality parameters, namely the relative thermal sensitivity (S_R) and the temperature uncertainty (δT). The S_R values were calculated by the following mathematical relation (Eq.(S6)):[1]

$$S_R = \frac{1}{\Delta}\left(\frac{\partial\Delta}{\partial T}\right) = \left(\frac{I_N}{I_M}\right)\left(\frac{\partial I_M/I_N}{\partial T}\right) \quad \text{(S6)}$$

while the δT values were obtained from the Eq.(S7):

$$\delta T = \frac{1}{S_R}\left(\frac{\delta\Delta}{\Delta}\right) \quad \text{(S7)}$$

Additional Figures

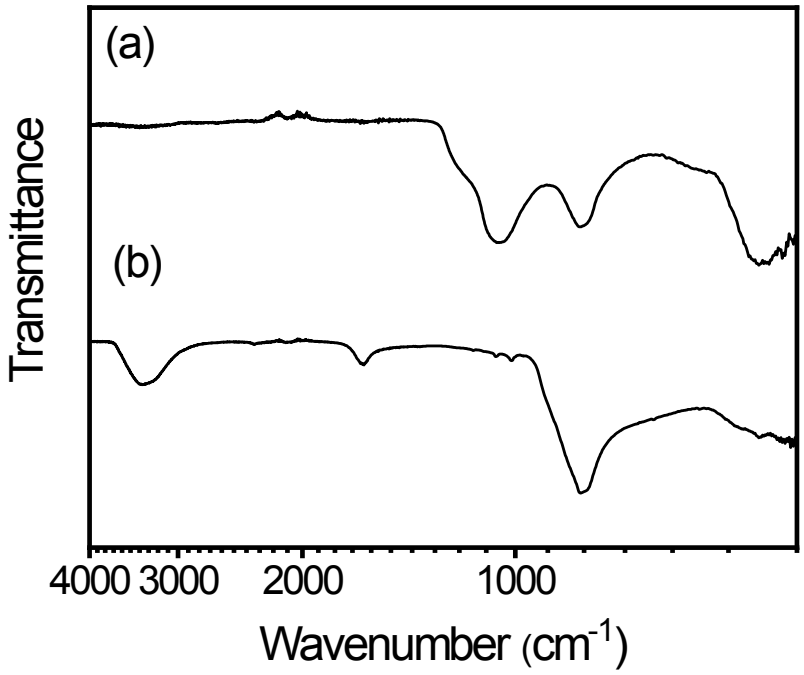

Figure. S1. Infrared spectra (ATR-FITR) of (a) as-synthesized and (b) final $Y_{0.77}Yb_{0.20}Tm_{0.02}Er_{0.01}VO_4$ nanoparticles after protected annealing and elimination of SiO_2 by HF for 30 min.

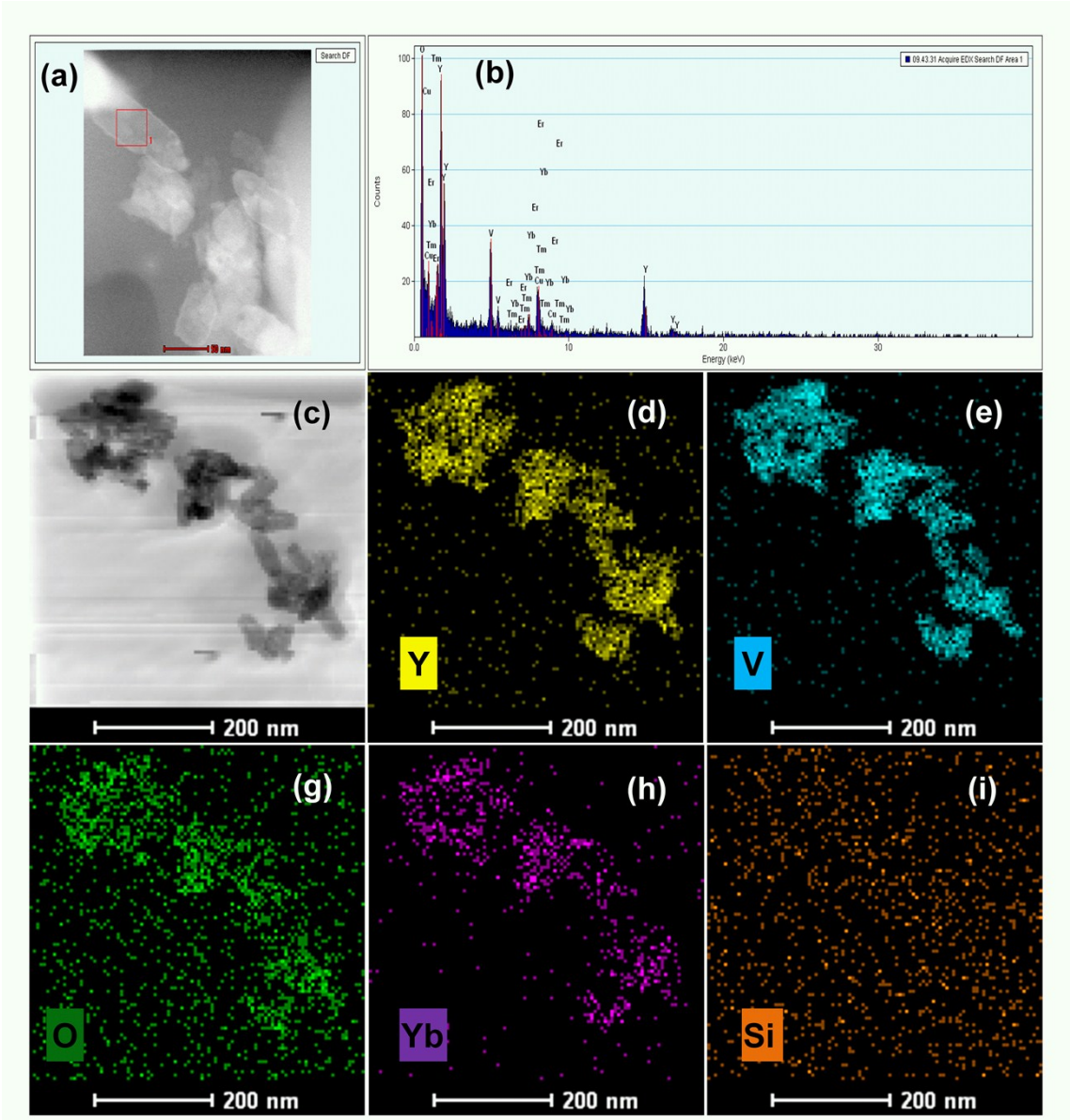

Figure. S2. (a),(b) EDS analysis of a representative part of the sample, (a) bright-field image and (b) EDS spectrum. (c)-(i) Elementary mapping of final $Y_{0.77}Yb_{0.20}Tm_{0.02}Er_{0.01}VO_4$ nanoparticles obtained after SiO_2 dissolution [Tm^{3+} and Er^{3+} could not be detected due to their low concentrations; Si signals on (i) is a consequence of noise. Scale bar on (a) corresponds to 50 nm].

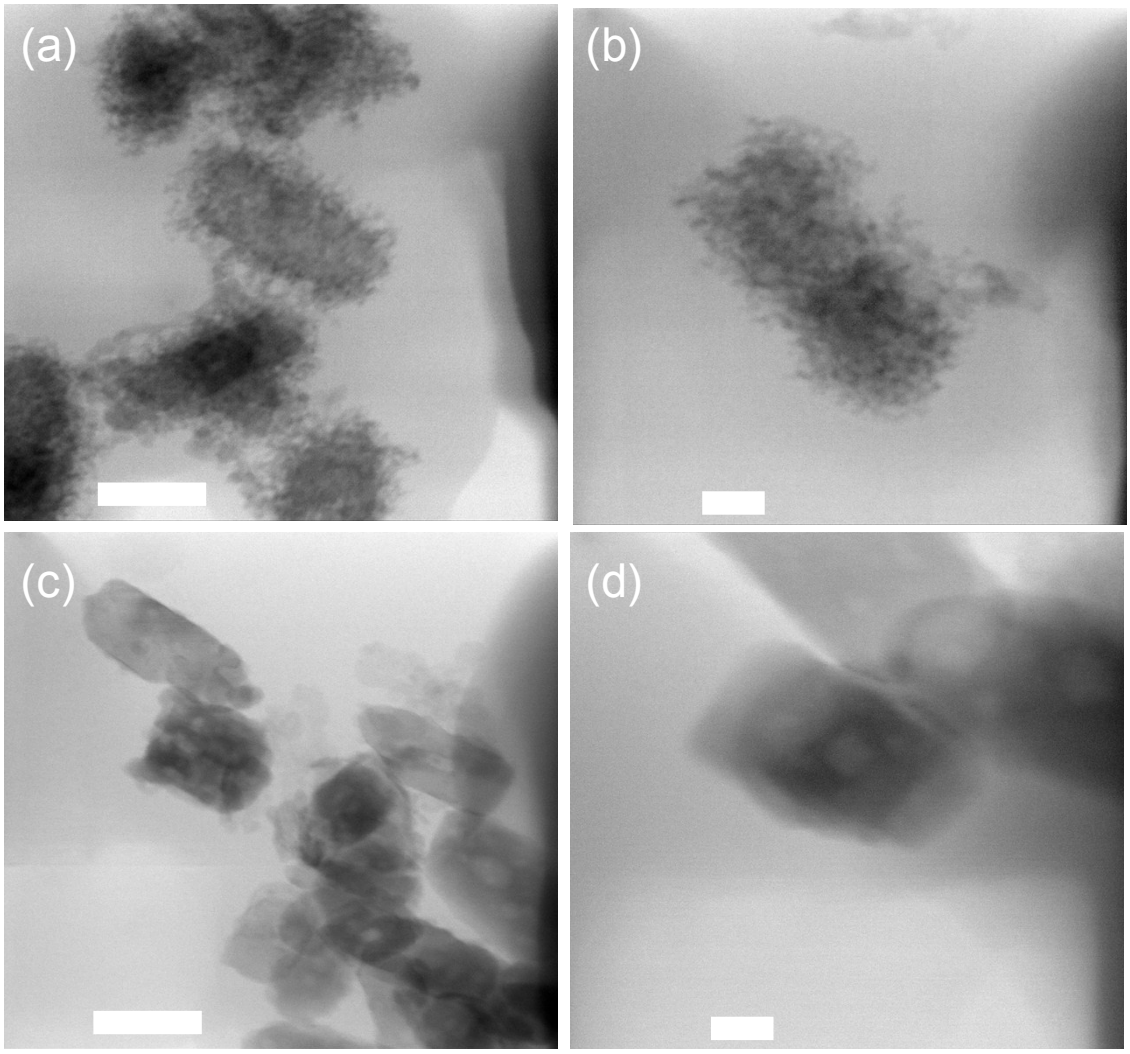

Figure S3. TEM images of (a),(b) as-synthesized and (c),(d) final $Y_{0.77}Yb_{0.20}Tm_{0.02}Er_{0.01}VO_4$ nanoparticles obtained after protected annealing and SiO_2 dissolution. Scale bars in (a),(c) and (b),(d) correspond to 50 and 20 nm, respectively. The layers covering the as-synthesized nanoparticles in (a),(b) correspond to the PAA polymer used to increase the colloidal stability.

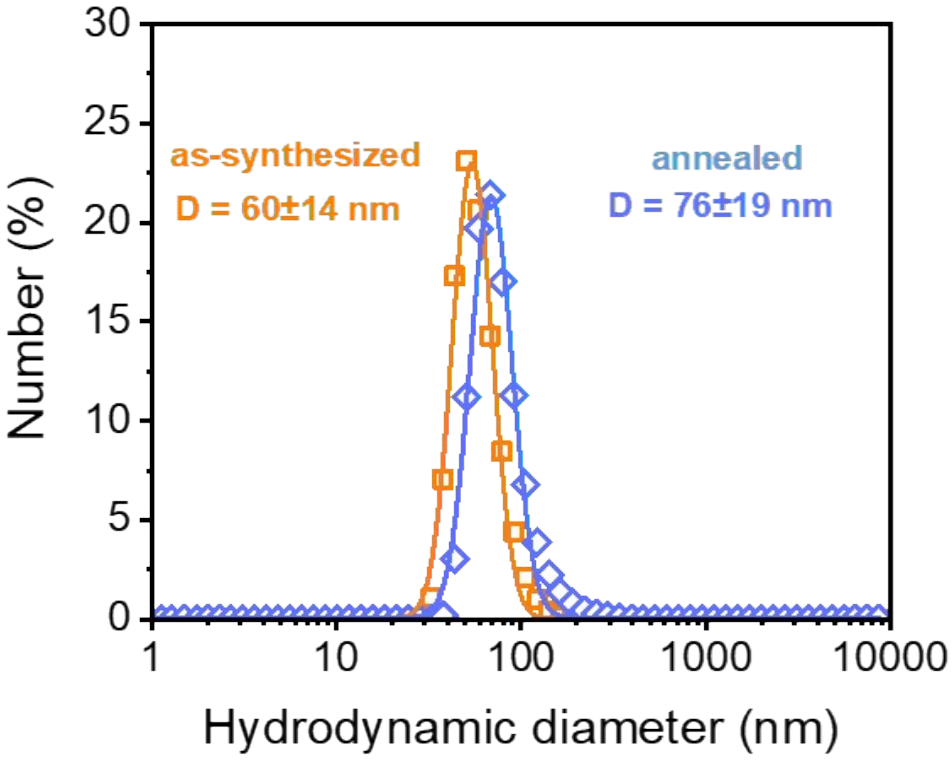

Figure. S4. Dynamic light scattering size distribution curves for as-synthesized (orange squares) and final (blue diamonds) $Y_{0.77}Yb_{0.20}Tm_{0.02}E_{0.01}VO_4$ particles obtained after annealing procedure and elimination of silica. The lines represent the mathematical fit of the experimental data using log-normal distributions (r^2 > 0.988). The prepared colloidal particles were stabilized with PAA polymer solution and dispersed in water (~0.5 mmol L^{-1} in $REVO_4$). The molar ratio V:PAA was 1:0.05.

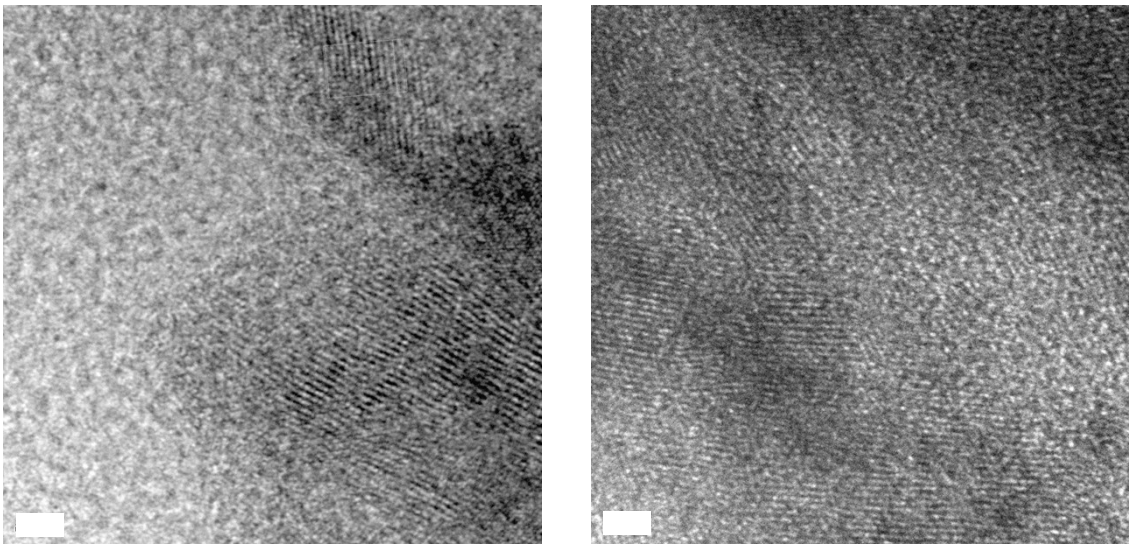

Figure. S5. HRTEM images of final $Y_{0.77}Yb_{0.20}Tm_{0.02}Er_{0.01}VO_4$ particles after silica dissolution evidencing the polycrystalline character of the solid. Scale bars correspond to 2 nm.

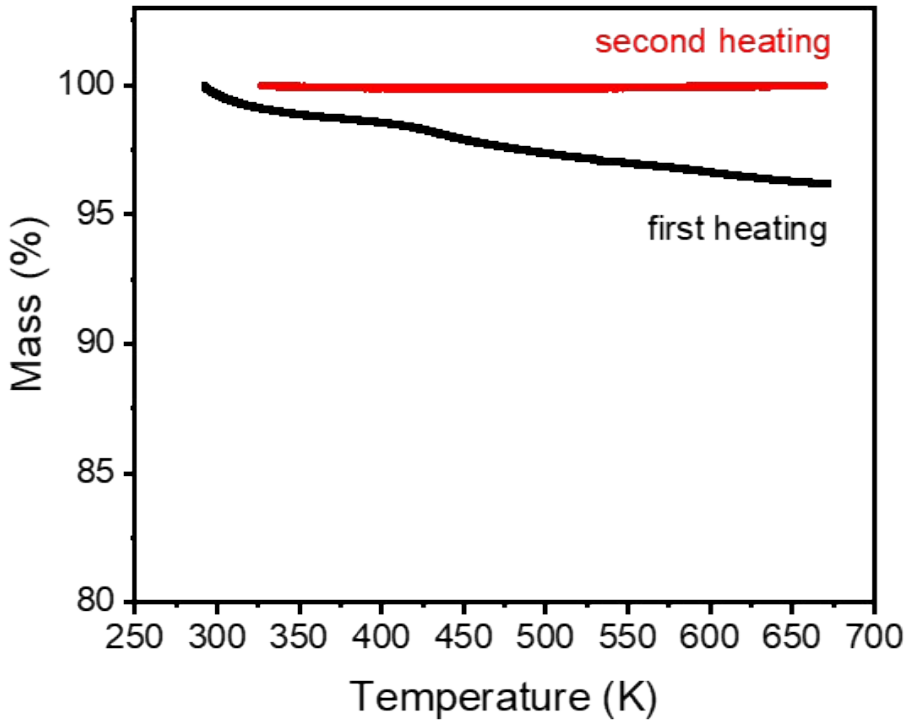

Figure. S6. Thermogravimetry (TGA) curves of final $Y_{0.77}Yb_{0.20}Tm_{0.02}Er_{0.01}VO_4$ particles in air. The first heating cycle is depicted in black, while the second heating cycle is represented in red. After the first heating process, the composition of the sample is constant.

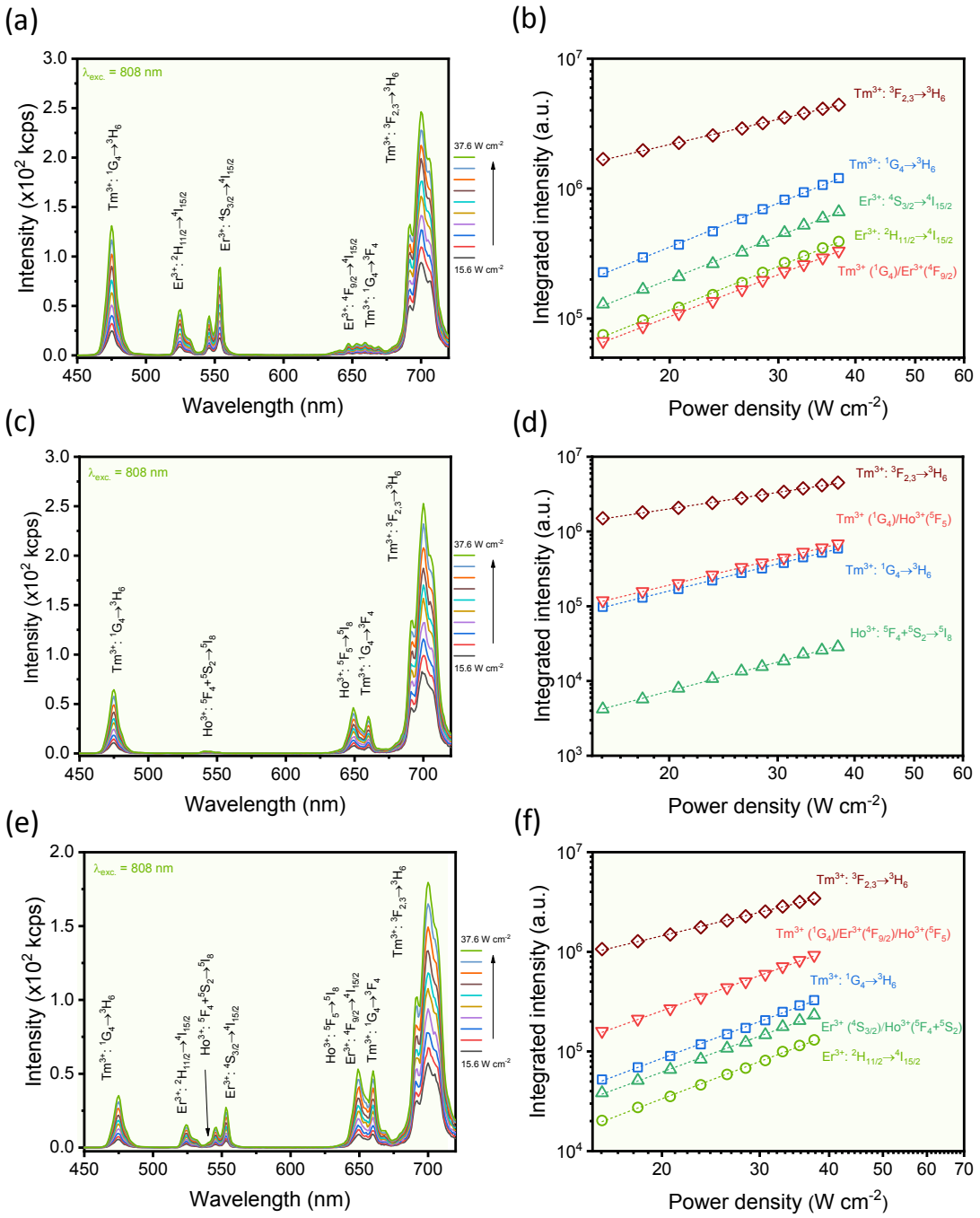

Figure. S7. (a),(c),(e) Upconversion spectra ($\lambda_{exc.}$ = 808 nm) and (b),(d),(f) dependence of the integrated intensities against excitation powers from 15.6 (dark gray) to 37.6 W cm^{-2} (green line) for (a),(b) $Y_{0.77}Yb_{0.20}Tm_{0.02}Er_{0.01}VO_4$, (c),(d) $Y_{0.772}Yb_{0.20}Tm_{0.025}Ho_{0.003}VO_4$, and (e),(f) $Y_{0.762}Yb_{0.20}Tm_{0.025}Er_{0.01}Ho_{0.003}VO_4$ particles. [(b): 476 nm (blue squares, slope=1.92), 526 nm (green circles, slope=1.91), 553 nm (green up triangles, slope=1.88), 658 nm (red down triangles, slope=1.83), and 700 nm (dark red diamonds, slope=1.10); (d): 476 nm (blue squares; slope=2.05), 541 nm (green up triangles, slope=2.20), 658 nm (red down triangles, slope=2.00), and 700 nm (dark red diamonds, slope=1.25); (f): 476 nm (blue squares; slope=2.10), 526 nm (green circles, slope=2.13), 553 nm (green up triangles, slope=2.12), 658 nm (red down triangles, slope=2.01), and 700 nm (dark red diamonds, slope=1.34)]. $r^2 > 0.998$.

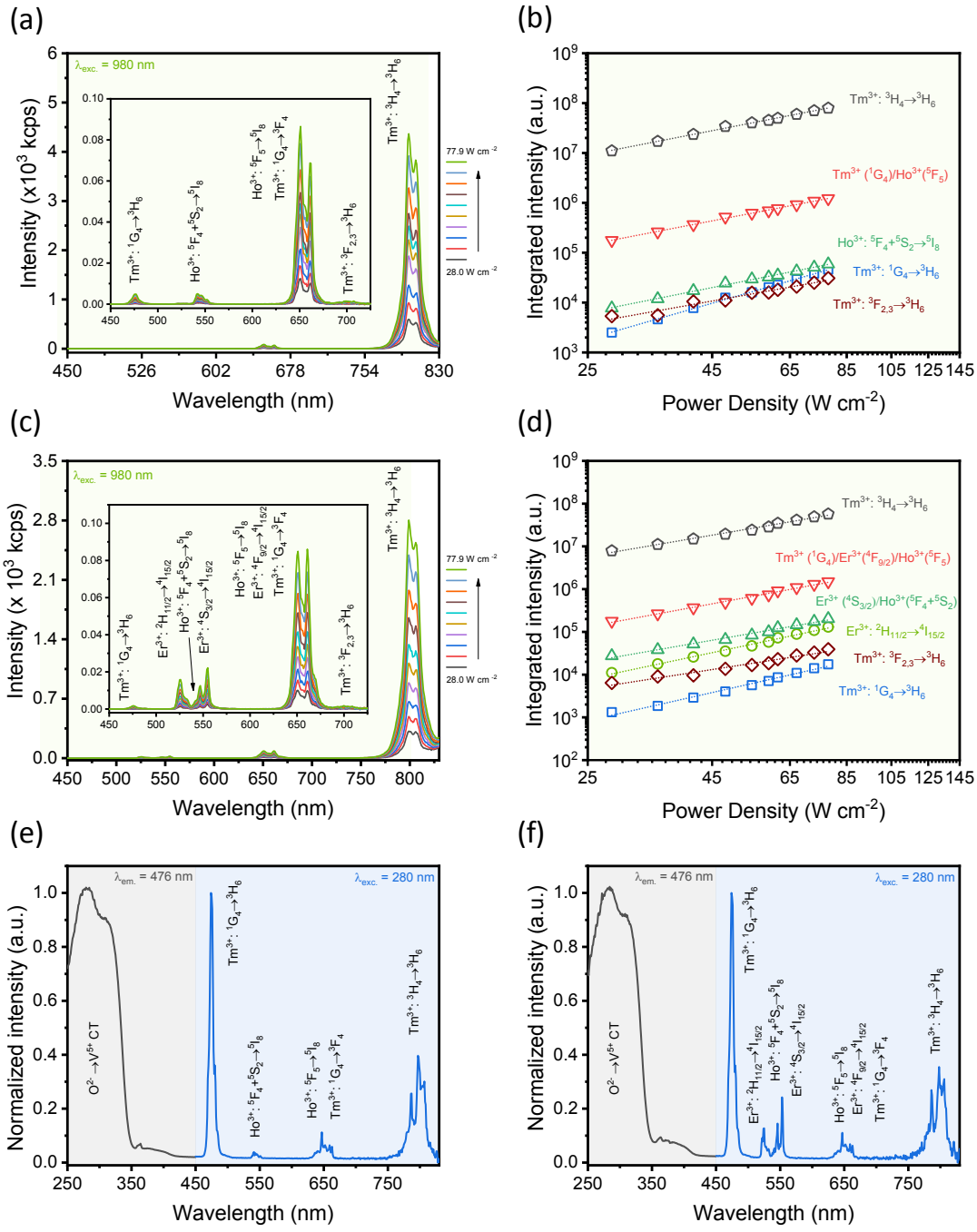

Figure. S8. (a),(c) Upconversion spectra ($\lambda_{exc.}$=980 nm) and (b),(d) dependence of the integrated intensities against excitation powers for (a),(b) $Y_{0.772}Yb_{0.20}Tm_{0.025}Ho_{0.003}VO_4$ and (c),(d) $Y_{0.762}Yb_{0.20}Tm_{0.025}Er_{0.01}Ho_{0.003}VO_4$ particles. (e),(f) Downshift excitation (λ_{em}=476 nm, left) and emission (λ_{exc}=280 nm, right) spectra of (e) $Y_{0.772}Yb_{0.20}Tm_{0.025}Ho_{0.003}VO_4$ and (f) $Y_{0.762}Yb_{0.20}Tm_{0.025}Er_{0.01}Ho_{0.003}VO_4$ particles. [(b): 476 nm (blue squares, slope=2.81), 541 nm (green up triangles, slope=1.95), 658 nm (red down triangles, slope=1.89), 700 nm (dark red diamonds, slope=1.75), and 801 nm (black pentagons, slope=1.91); (d): 476 nm (blue squares, slope=2.68), 526 nm (green circles, slope=2.32), 553 nm (green up triangles, slope=1.99), 658 nm (red down triangles, slope=2.10), 700 nm (dark red diamonds, slope=1.77) and 801 nm (black pentagons, slope=1.92); correlation coefficients (r^2) ranged between 0.971 and 0.999].

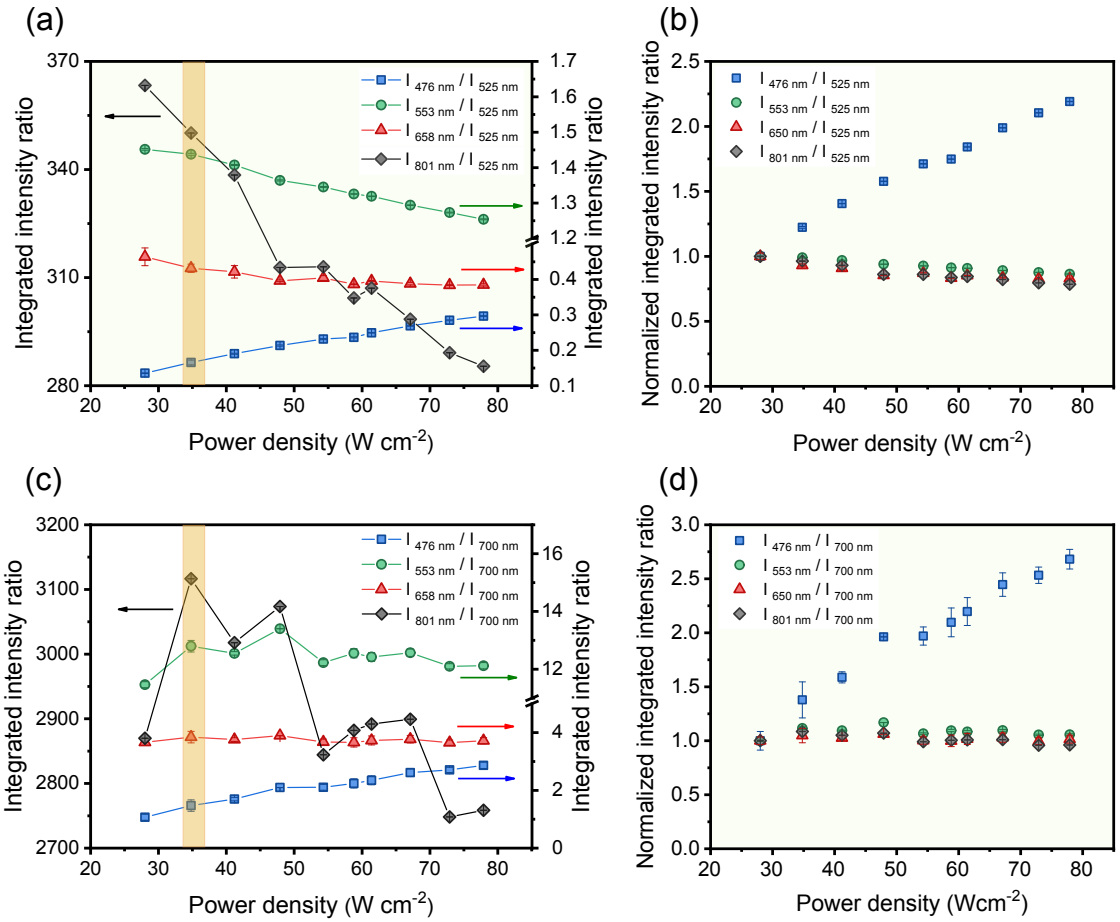

Figure. S9. Dependence of different intensity ratios against excitation powers (λ_{exc} = 980 nm) for $Y_{0.77}Yb_{0.20}Tm_{0.02}Er_{0.01}VO_4$ powder particles. The integrated intensity ratios were considered using the $I_{525\ nm}$ [$^2H_{11/2}\rightarrow{}^4I_{15/2}$ of Er^{3+}; (a),(b)] and $I_{700\ nm}$ [$^3F_{2.3}\rightarrow{}^3H_6$ of Tm^{3+}; (c),(d)] emissions for comparison. The $I_{476\ nm}$, $I_{553\ nm}$, $I_{658\ nm}$, and $I_{801\ nm}$ labels refer to the integrated intensities of the $^1G_4\rightarrow{}^3H_6$ (Tm^{3+}), $^4S_{3/2}\rightarrow{}^4I_{15/2}$ (Er^{3+}), $^1G_4\rightarrow{}^3F_4$ + $^4F_{9/2}\rightarrow{}^4I_{15/2}$ (Tm^{3+} + Er^{3+}), and $^3H_4\rightarrow{}^3H_6$ (Tm^{3+}) transitions, respectively. (a) and (c) show integrated intensity ratio values; in (b) and (d), the values from (a) and (c) at 28 W cm^{-2} were normalized to 1 and the remaining were represented accordingly. The highlighted ranges denoted in (a),(c) depicted the power density used on the temperature dependent measurements (34.8 W cm^{-2}).

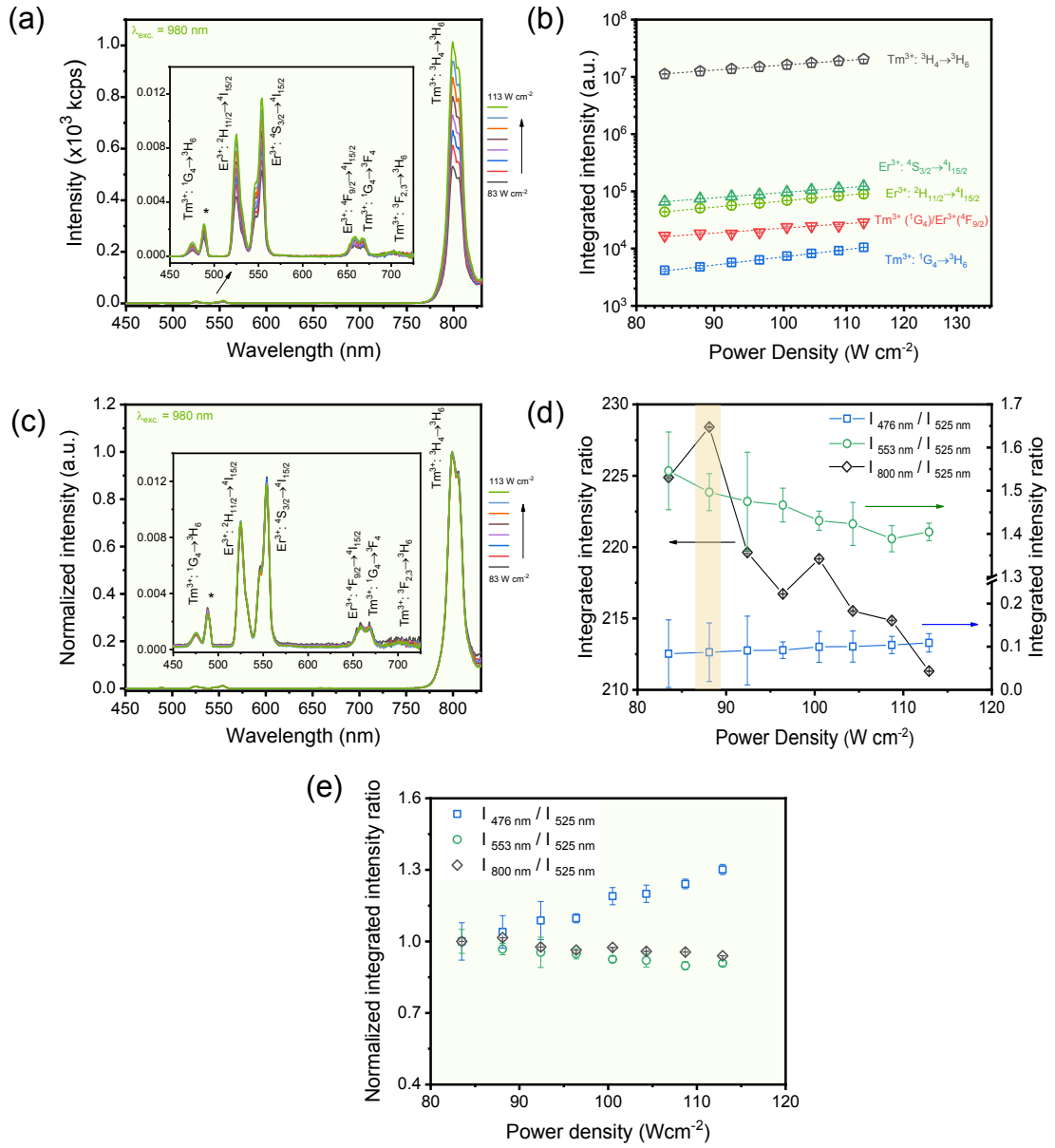

Figure. S10. Dependence of luminescence of final $Y_{0.77}Yb_{0.20}Tm_{0.02}Er_{0.01}VO_4$ colloidal nanoparticles (λ_{exc} = 980 nm) against pump powers. (a),(c) Upconversion spectra and (b) dependence of the integrated intensities against excitation powers ranging from 83 (dark gray) to 113 W cm^{-2} (green line). The emissions considered were 476 nm (blue squares; slope=3.12), 526 nm (green circles, slope=2.42), 553 nm (green up triangles, slope=2.05), 658 nm (red down triangles, slope=1.89), and 801 nm (black pentagons, slope=1.96); $r^2 > 0.997$. (d),(e) Dependence of different intensity ratios against pump powers using the I_{525} ($^2H_{11/2}\rightarrow{}^4I_{15/2}$ of Er^{3+}) emission for comparison. The highlighted range in (d) depicts the pump power used on temperature dependent measurements (88 W cm^{-2}) in colloids; in (e) intensity ratio values under the lowest pump power were normalized to 1. Asterisks in (a),(c) correspond to the laser overtone line (489 nm), which was not considered in data processing.

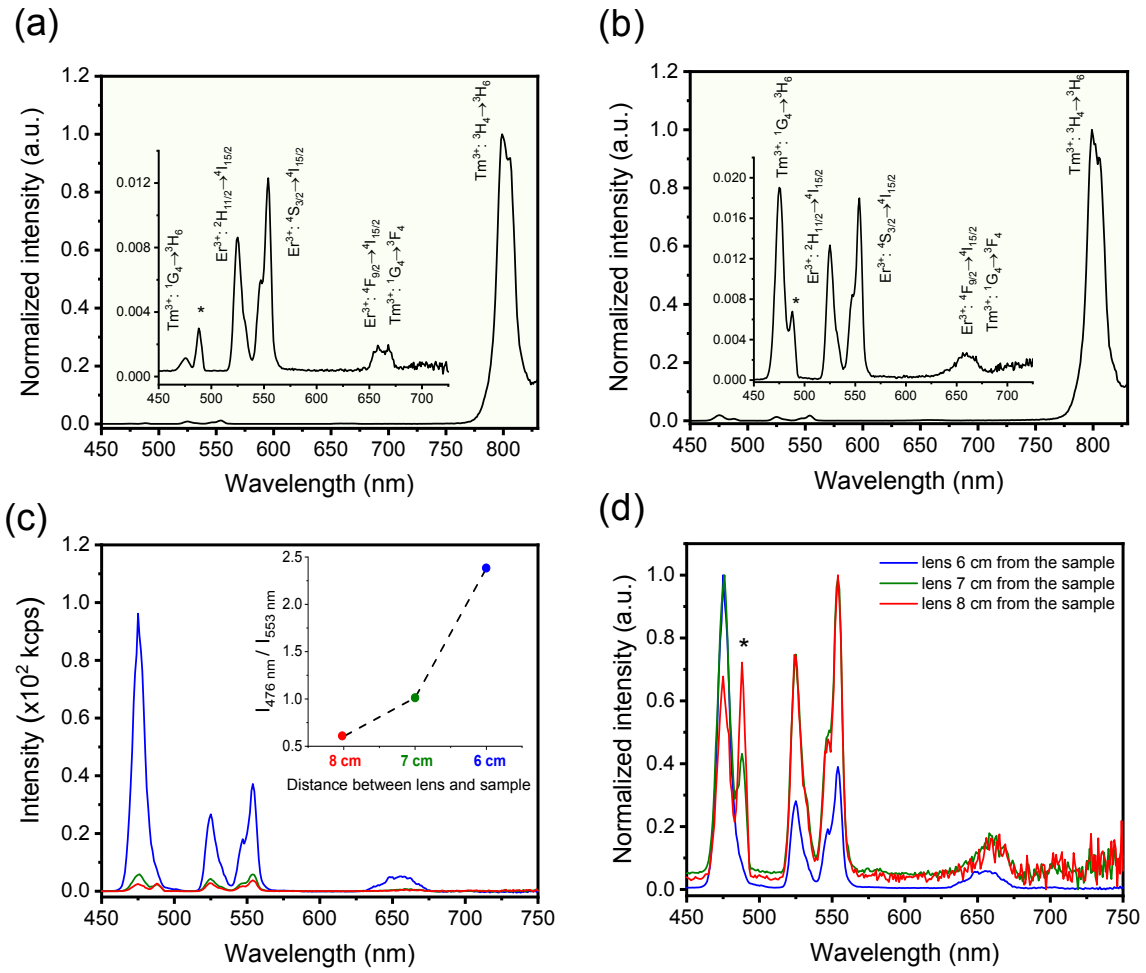

Figure. S11. Influence of focusing elements for laser beam on the emission profile of $Y_{0.77}Yb_{0.20}Tm_{0.02}Er_{0.01}VO_4$ colloidal particles. Upconversion spectra (λ_{exc}=980 nm) in (a) absence and (b) presence of a convergent lens. (c),(d) Effect of the alteration of the distance between lens and sample on the spectral profile. The lens was positioned in different distances, namely 6 (blue), 7 (green) and 8 cm (red) from the sample. The concentration of the suspension, nominal pump power and optical path were kept constant during all measurements [50 mmol L^{-1}, 400 mW and 1 cm, respectively]. The inset in (c) shows the variation of the absolute intensity ratio I_{476}/I_{553} against lens-sample distance. The I_{476} and I_{553} labels correspond to the $^1G_4 \rightarrow {}^3H_6$ and $^2H_{11/2} \rightarrow {}^4I_{15/2}$ transitions of Tm^{3+} and Er^{3+}, respectively. Asterisks in (a),(b),(d) correspond to the laser overtone line (489 nm).

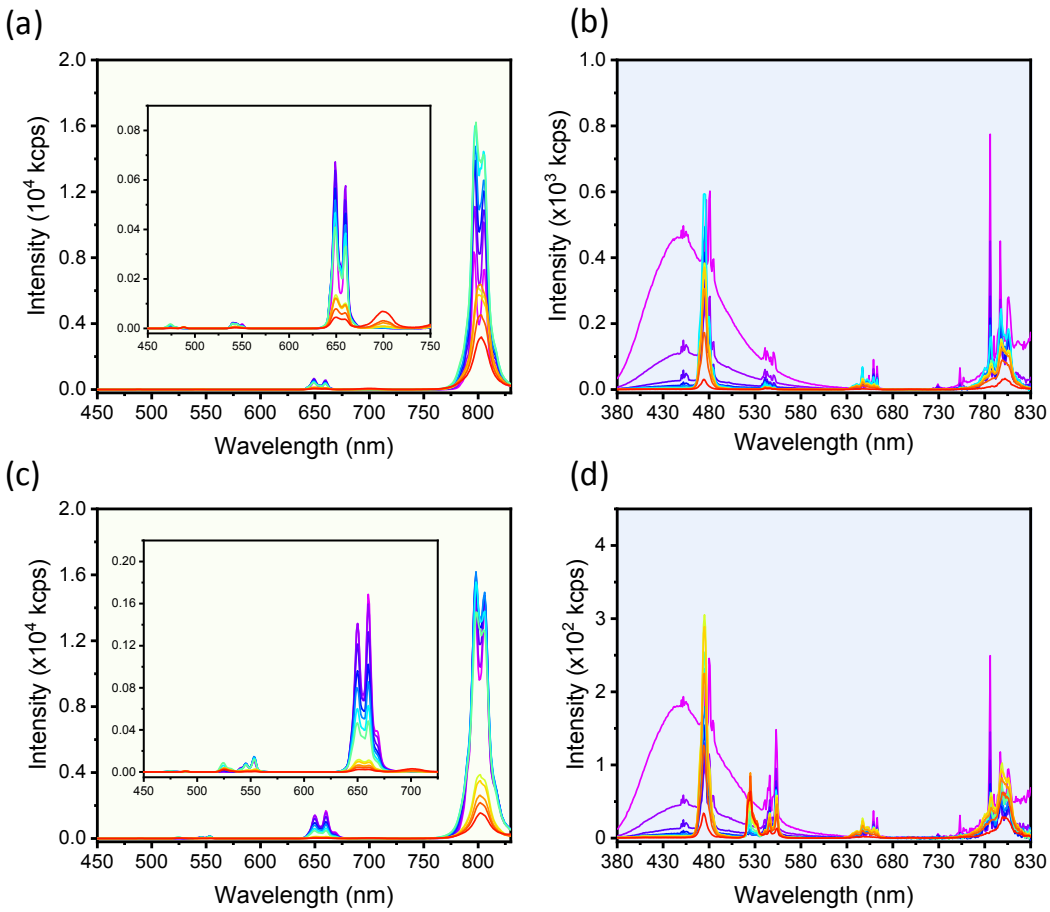

Figure. S12. Temperature dependent (a),(c) upconversion ($\lambda_{exc.}$=980 nm, P=34.8 W cm^{-2}) and (b),(d) downshift ($\lambda_{exc.}$=280 nm) spectra of (a),(b) $Y_{0.772}Yb_{0.20}Tm_{0.025}Ho_{0.003}VO_4$ and (c),(d) $Y_{0.762}Yb_{0.20}Tm_{0.025}Er_{0.01}Ho_{0.003}VO_4$ particles as powders. Colours denote temperatures from 77 K (violet) to 673 K (red) [77, 117, 157, 197, 237, 277, 318, 343, 373, 433, 503 and 673 K].

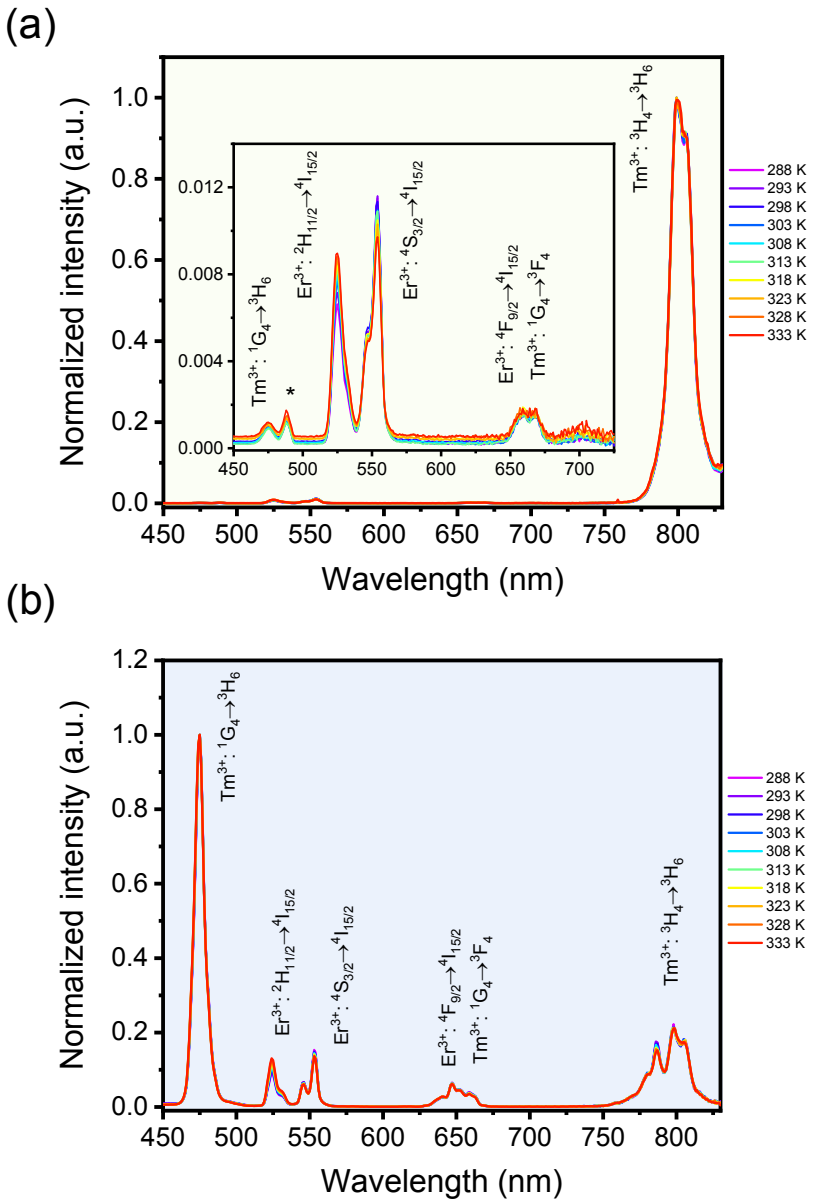

Figure. S13. Temperature dependent (a) upconversion ($\lambda_{exc.}$=980 nm, P=88 W cm^{-2}) and (b) downshift ($\lambda_{exc.}$=280 nm) spectra of $Y_{0.77}Yb_{0.20}Tm_{0.02}Er_{0.01}VO_4$ colloidal particles [50 mmol L^{-1}, 3 mL and optical path of 1 cm]. Asterisk in (a) corresponds to the laser overtone line (489 nm), which was not considered in data processing.

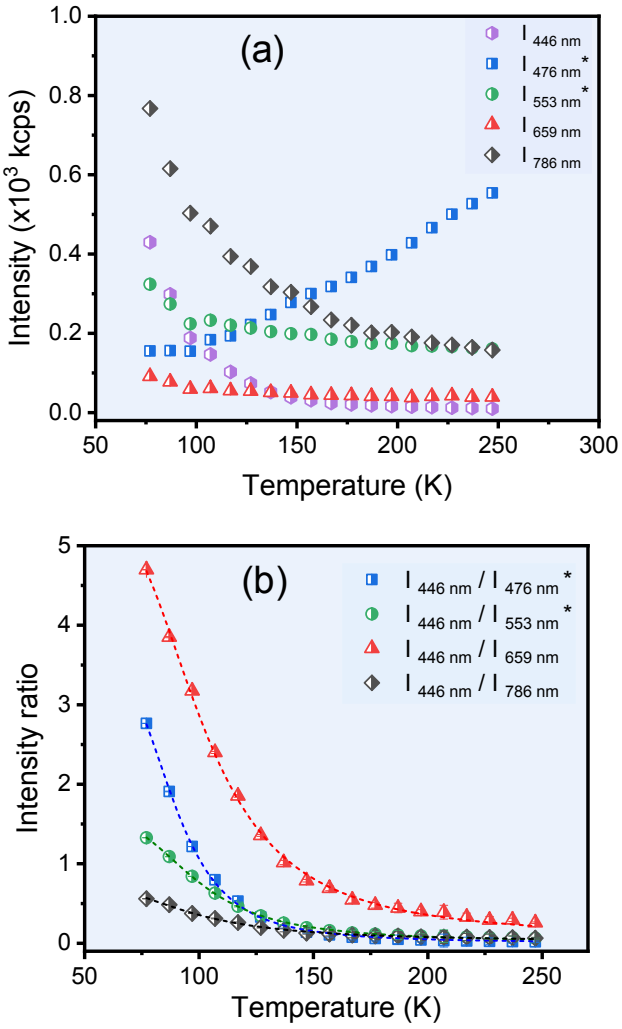

Figure. S14. Dependence of (a) absolute intensities and (b) ratios between absolute intensities against temperature for $Y_{0.77}Yb_{0.20}Tm_{0.02}Er_{0.01}VO_4$ powder particles under UV excitation (λ_{exc}=280 nm). The $I_{446\ nm}$, $I_{476\ nm}$, $I_{553\ nm}$, $I_{659\ nm}$, and $I_{786\ nm}$ labels refer to the absolute intensities of the $^3T_{2,1}\rightarrow{}^1A_1$ (VO_4^{3-}), $^1G_4\rightarrow{}^3H_6$ (Tm^{3+}), $^4S_{3/2}\rightarrow{}^4I_{15/2}$ (Er^{3+}), $^1G_4\rightarrow{}^3F_4$ + $^4F_{9/2}\rightarrow{}^4I_{15/2}$ (Tm^{3+} + Er^{3+}), and $^3H_4\rightarrow{}^3H_6$ (Tm^{3+}) transitions, respectively. The $I_{476\ nm}$* and $I_{553\ nm}$* labels correspond to the absolute intensities at 476 and 553 nm after baseline correction [$I_{476\ nm}$* = $I_{476\ nm}$ - $I_{462\ nm}$; and $I_{553\ nm}$* = $I_{553\ nm}$ - $I_{600\ nm}$]. Fitting parameters obtained in (b) are presented in Table S3.

Table 1. Fitting parameters obtained from the dependence of the intensity ratios [(I_M/I_N)] on the absolute temperature for the different emissions in final $Y_{0.77}Yb_{0.20}Tm_{0.02}Er_{0.01}VO_4$ particles as powders and colloids. Experimental data were fitted by Eq.(S1), that displays the form (I_M/I_N)= A exp(-B/T); r^2 denotes correlation coefficients and ΔE the theoretical energy differences on the $\Delta E/K_B$ term of Eq.(S1)

Intensity ratio	Experimental setup[1]	r^2	A	B (K)	ΔE (cm^{-1})
Powder ($\lambda_{exc.}$ = 980 nm)					
$I_{476\ nm}$ / $I_{525\ nm}$	Low temperature	0.999	1.57×10^{-2}	713	496
	High temperature	0.999	4.65×10^{-3}	866	602
$I_{553\ nm}$ / $I_{525\ nm}$	Low temperature	0.995	1.62×10^{-1}	754	524
	High temperature	0.999	7.05×10^{-2}	823	572
$I_{658\ nm}$ / $I_{525\ nm}$	Low temperature	0.999	3.68×10^{-2}	830	577
	High temperature	0.999	3.32×10^{-2}	647	450
$I_{801\ nm}$ / $I_{525\ nm}$	Low temperature	0.999	2.80×10^{1}	837	582
	High temperature	0.997	2.63×10^{1}	664	461
Powder ($\lambda_{exc.}$ = 980 nm)					
$I_{476\ nm}$ / $I_{700\ nm}$	Low temperature	0.997	3.24×10^{-3}	1766	1227
	High temperature	0.999	4.41×10^{-4}	2260	1571
$I_{553\ nm}$ / $I_{700\ nm}$	Low temperature	0.999	1.79×10^{-2}	1948	1354
	High temperature	0.998	5.70×10^{-3}	2250	1564
$I_{658\ nm}$ / $I_{700\ nm}$	Low temperature	0.999	5.58×10^{-3}	1959	1362
	High temperature	0.999	3.11×10^{-3}	2021	1405
$I_{801\ nm}$ / $I_{700\ nm}$	Low temperature	0.999	4.40×10^{0}	1960	1362
	High temperature	0.999	2.66×10^{0}	2009	1396
Powder ($\lambda_{exc.}$ = 280 nm)					
$I_{553\ nm}$ / $I_{525\ nm}$	Low temperature	0.996	8.90×10^{-2}	839	581
	High temperature	0.999	5.30×10^{-2}	989	687
Colloid ($\lambda_{exc.}$ = 980 nm)					
$I_{476\ nm}$ / $I_{525\ nm}$	-	0.995	1.48×10^{-3}	1240	862
$I_{553\ nm}$ / $I_{525\ nm}$	-	0.998	1.09×10^{-1}	810	563
$I_{801\ nm}$ / $I_{525\ nm}$	-	0.996	2.08×10^{1}	749	521
Colloid ($\lambda_{exc.}$ = 280 nm)					
$I_{476\ nm}$ / $I_{525\ nm}$	-	0.999	8.88×10^{-1}	760	528
$I_{553\ nm}$ / $I_{525\ nm}$	-	0.999	5.78×10^{-2}	954	663
$I_{658\ nm}$ / $I_{525\ nm}$	-	0.997	8.34×10^{-2}	841	585
$I_{801\ nm}$ / $I_{525\ nm}$	-	0.996	4.45×10^{-1}	815	566

[1]Temperature-dependent upconversion and downshift spectra of the particles as powders were performed using two experimental setups. For temperatures lower than 318 K, the sample was placed in a cryostat coupled to the spectrofluorometer; for temperatures higher than 318 K, the sample was put in a platinum crucible of a temperature-controlled stage. Details are described in previous sections.

Table S2. Fitting parameters obtained from the dependence of the intensity ratios [(I_M/I_N)] on the absolute temperature for the different emissions in final $Y_{0.77}Yb_{0.20}Tm_{0.02}Er_{0.01}VO_4$ particles as powders under excitation at $\lambda_{exc.}$ = 280 nm. Experimental data were fitted by Eq.(S2), that displays the form $(I_{Ln^{3+}}/I_{VO_4^{3-}})$ = A*[1+Bexp(−C/T)]./[1+Dexp(−E/T)]; r^2 denotes correlation coefficients and ΔE the theoretical energy differences on the $\Delta E/K_B$ terms of Eq.(S2)

	r^2	A	B	C (K)	ΔE_C (cm^{-1})	D	E (K)	ΔE_E (cm^{-1})
Powder ($\lambda_{exc.}$ = 280 nm)								
$I_{476\ nm}/I_{380\text{-}510\ nm}$	0.999	3.05×10^{-1}	1.06×10^{2}	637	443	3.48×10^{1}	680	472
$I_{553\ nm}/I_{380\text{-}510\ nm}$	0.999	7.30×10^{-2}	5.27×10^{1}	460	320	2.47×10^{2}	1035	719
$I_{658\ nm}/I_{380\text{-}510\ nm}$	0.999	1.27×10^{-1}	4.45×10^{-4}	1008	701	3.44×10^{-4}	1191	827
$I_{786\ nm}/I_{380\text{-}510\ nm}$	0.997	6.22×10^{-1}	2.02×10^{-4}	1076	748	4.00×10^{-4}	1109	771

Table S3. Fitting parameters obtained from the dependence of the intensity ratios [(I_M/I_N)] on the absolute temperature for the different emissions in final $Y_{0.77}Yb_{0.20}Tm_{0.02}Er_{0.01}VO_4$ particles as powders under excitation at $\lambda_{exc.}$ = 280 nm. Experimental data were fitted by Eq.(S3), that presents the form $\left(\frac{I_{VO_4^{3-}}}{I_{Ln^{3+}}}\right)$ = A/[1+Bexp(−C/T)]; r^2 denotes correlation coefficients and ∆E the theoretical energy differences on the $\Delta E/K_B$ term of Eq.(S3)

	r^2	A	B	C (K)	ΔE (cm^{-1})
Powder ($\lambda_{exc.}$ = 280 nm)					
$I_{446\ nm} / I_{476\ nm}$	0.999	3.63×10^0	2122	678	471
$I_{446\ nm} / I_{553\ nm}$	0.999	1.60×10^0	305	564	392
$I_{446\ nm} / I_{658\ nm}$	0.999	5.51×10^0	227	551	383
$I_{446\ nm} / I_{786\ nm}$	0.996	7.55×10^{-1}	68	411	286

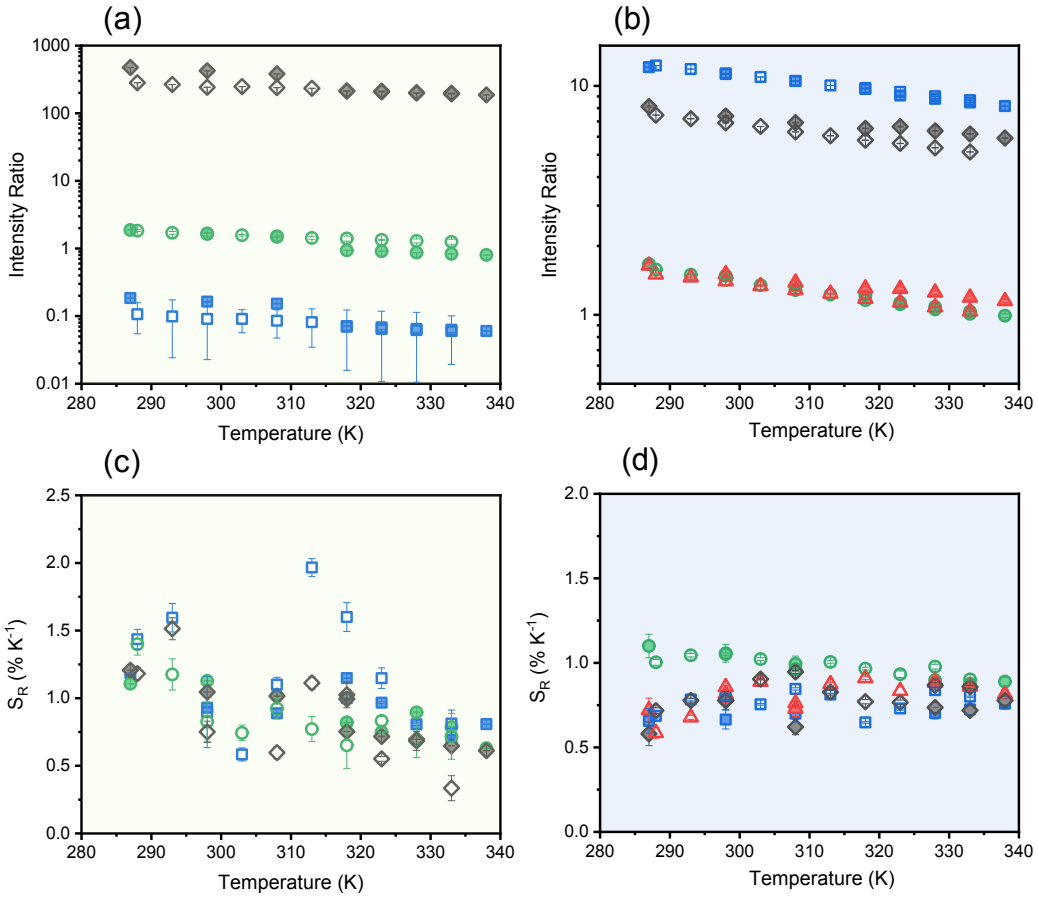

Figure S15. Comparison between the thermometric response [(a),(b) integrated intensity ratio and (c),(d) relative thermal sensitivity, S_R] obtained for $Y_{0.77}Yb_{0.20}Tm_{0.02}Er_{0.01}VO_4$ particles as powders (filled symbols) and colloids (open symbols) under (a),(c) NIR (λ_{exc}=980 nm) and (b),(d) UV (λ_{exc}=280 nm) excitation. The symbols correspond to the I_{476}/I_{525} (blue squares), I_{553}/I_{525} (green circles), I_{658}/I_{525} (up triangles), and I_{801}/I_{525} (black diamonds) intensity ratios.

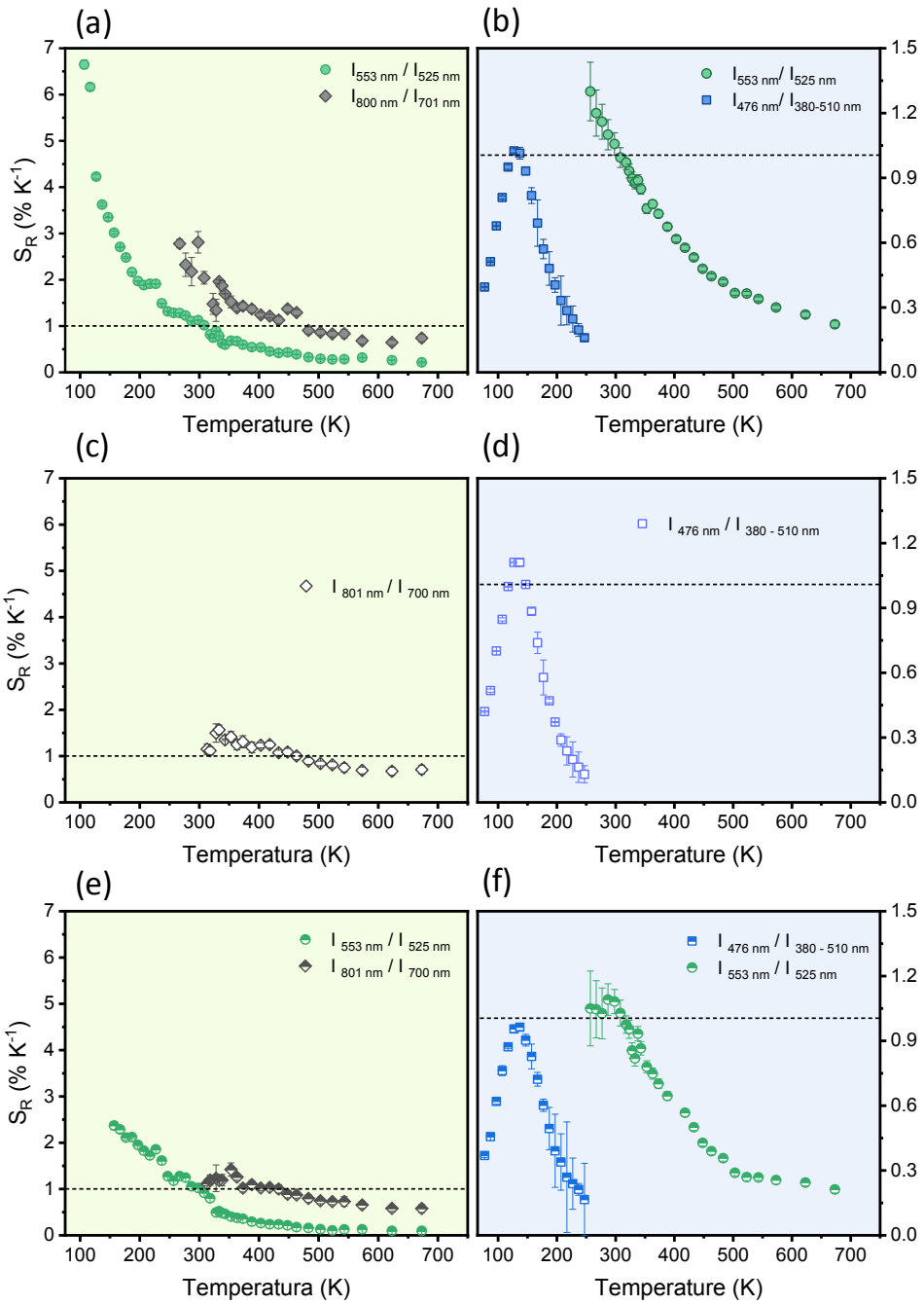

Figure. S16. Comparison between some relative thermal sensitivities (S_R) of (a),(b) $Y_{0.77}Yb_{0.20}Tm_{0.02}Er_{0.01}VO_4$, (c),(d) $Y_{0.772}Yb_{0.20}Tm_{0.025}Ho_{0.003}VO_4$, and (e),(f) $Y_{0.762}Yb_{0.20}Tm_{0.025}Er_{0.01}Ho_{0.003}VO_4$ particles under excitation at $\lambda_{exc.}$ = 980 nm (a,c,e) and 280 nm (b,d,f). Different emissions (indicated at the figures) were considered in each case, using the I_{525} ($^2H_{11/2}\rightarrow{}^4I_{15/2}$ of Er^{3+},], I_{700} [$^3F_{2.3}\rightarrow{}^3H_6$ of Tm^{3+}], and $I_{380\text{-}510}$ [$^3T_{2,1}\rightarrow{}^1A_1$ of VO_4^{3-}] emissions for comparison. The I_{553} and I_{801} labels refer to the integrated intensities of the $^4S_{3/2}\rightarrow{}^4I_{15/2}$ (Er^{3+}) and $^3H_4\rightarrow{}^3H_6$ (Tm^{3+}) transitions, respectively.

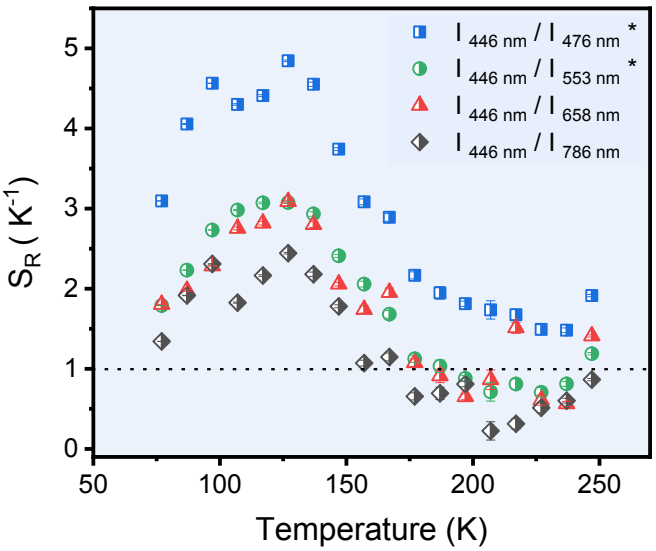

Figure. S17. Dependence of relative thermal sensitivities (S_R) on temperature for $Y_{0.77}Yb_{0.20}Tm_{0.02}Er_{0.01}VO_4$ powder particles under excitation at $\lambda_{exc.}$ = 280 nm considering ratios between absolute intensities instead of integrated intensities. The ratios were calculated using the $I_{446\,nm}$ emission for comparison, which corresponds to the $^3T_{2,1}\rightarrow{}^1A_1$ transitions of VO_4^{3-} group. The $I_{476\,nm}$, $I_{553\,nm}$, $I_{658\,nm}$, and $I_{786\,nm}$ labels refer to the absolute intensities of the $^1G_4\rightarrow{}^3H_6$ (Tm^{3+}), $^4S_{3/2}\rightarrow{}^4I_{15/2}$ (Er^{3+}), $^1G_4\rightarrow{}^3F_4$ + $^4F_{9/2}\rightarrow{}^4I_{15/2}$ (Tm^{3+} + Er^{3+}), and $^3H_4\rightarrow{}^3H_6$ (Tm^{3+}) transitions, respectively. The $I_{476\,nm}$* and $I_{553\,nm}$* labels correspond to the absolute intensity at 476 and 553 nm after baseline correction [$I_{476\,nm}$* = $I_{476\,nm}$ - $I_{462\,nm}$; and $I_{553\,nm}$* = $I_{553\,nm}$ - $I_{600\,nm}$].

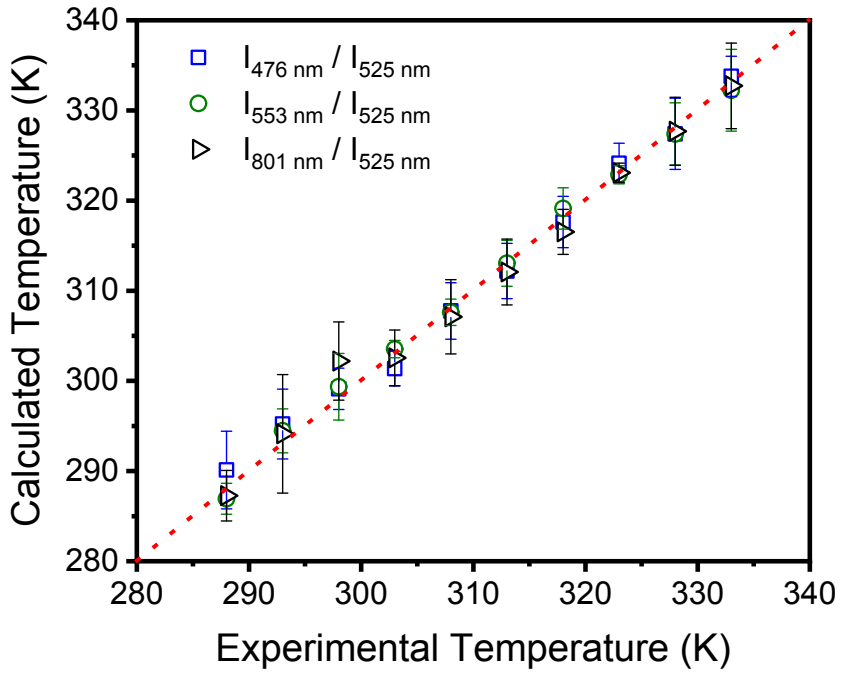

Figure S18. Relation between real temperatures and temperatures calculated using the calibration shown in Figure 4 and Table S1 for $Y_{0.77}Yb_{0.20}Tm_{0.02}Er_{0.01}VO_4$ colloidal particles (λ_{exc} = 980 nm). Real temperatures were measured using a mercury thermometer (±0.5 K) inside sample cells. The dashed line is a guide to the eye corresponding to the y = x function.

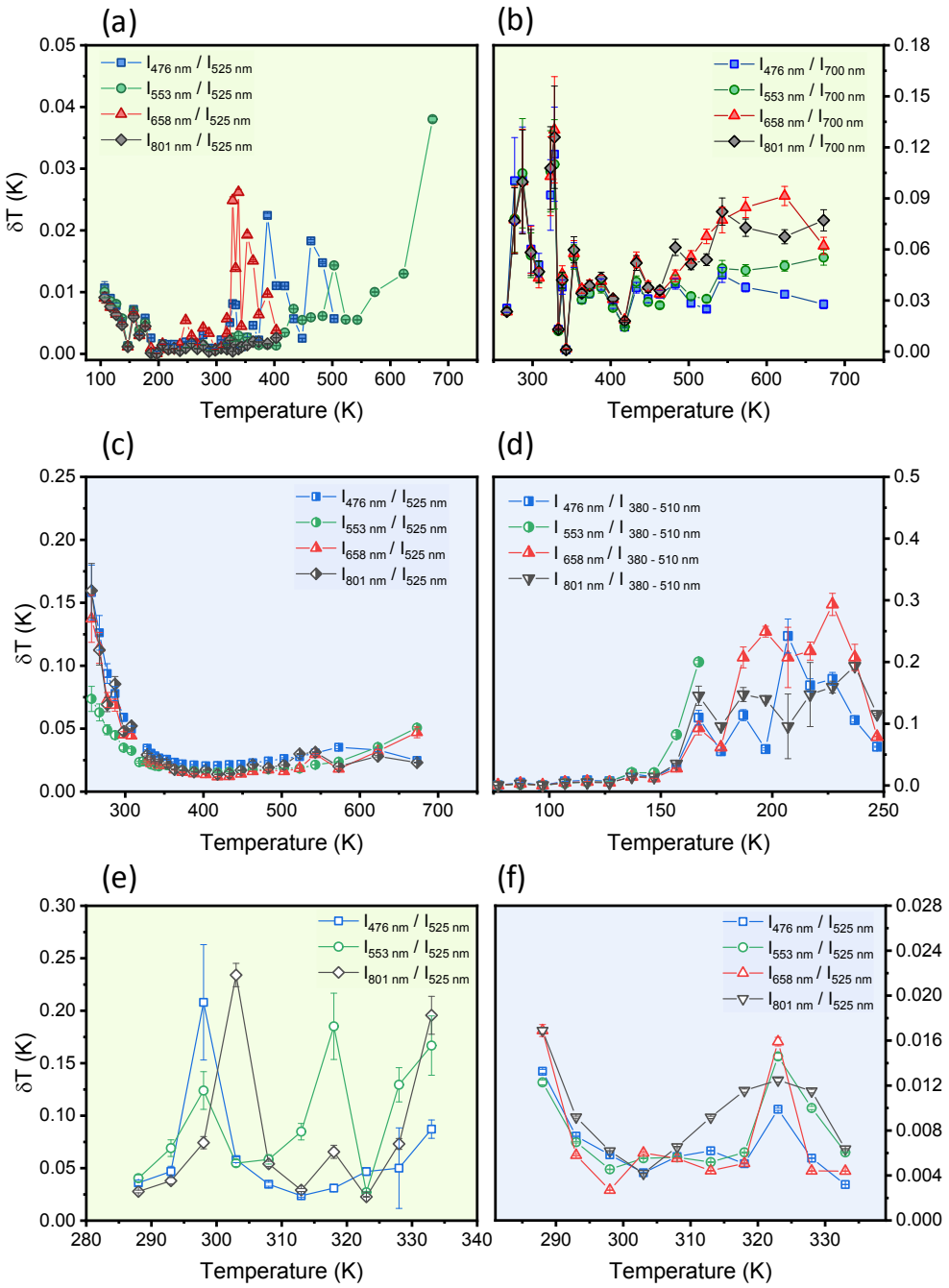

Figure. S19. Dependence of temperature uncertainty (δT) against the temperature for $Y_{0.77}Yb_{0.20}Tm_{0.02}Er_{0.01}VO_4$ particles as (a-d) powders (filled symbols) or (e,f) colloids (open symbols) under excitation at (a,b,e) $\lambda_{exc.}$ = 980 nm (upconversion, green background) and (c,d,f) $\lambda_{exc.}$ = 280 nm (downshift, blue background). Different emissions (indicated at the figures) were considered in each case, using the $I_{525\,nm}$ [$^2H_{11/2}\rightarrow{}^4I_{15/2}$ of Er^{3+}, (a), (c), (e) and (f)], $I_{700\,nm}$ [$^3F_{2,3}\rightarrow{}^3H_6$ of Tm^{3+}, (b)], and $I_{380\text{-}510\,nm}$ [$^3T_{2,1}\rightarrow{}^1A_1$ of VO_4^{3-}, (d)] emissions for comparison. The I_{476}, I_{553}, I_{658}, and I_{801} labels refer to the integrated intensities of the $^1G_4\rightarrow{}^3H_6$ (Tm^{3+}), $^4S_{3/2}\rightarrow{}^4I_{15/2}$ (Er^{3+}), $^1G_4\rightarrow{}^3F_4$ + $^4F_{9/2}\rightarrow{}^4I_{15/2}$ (Tm^{3+} and Er^{3+}), and $^3H_4\rightarrow{}^3H_6$ (Tm^{3+}) transitions, respectively.

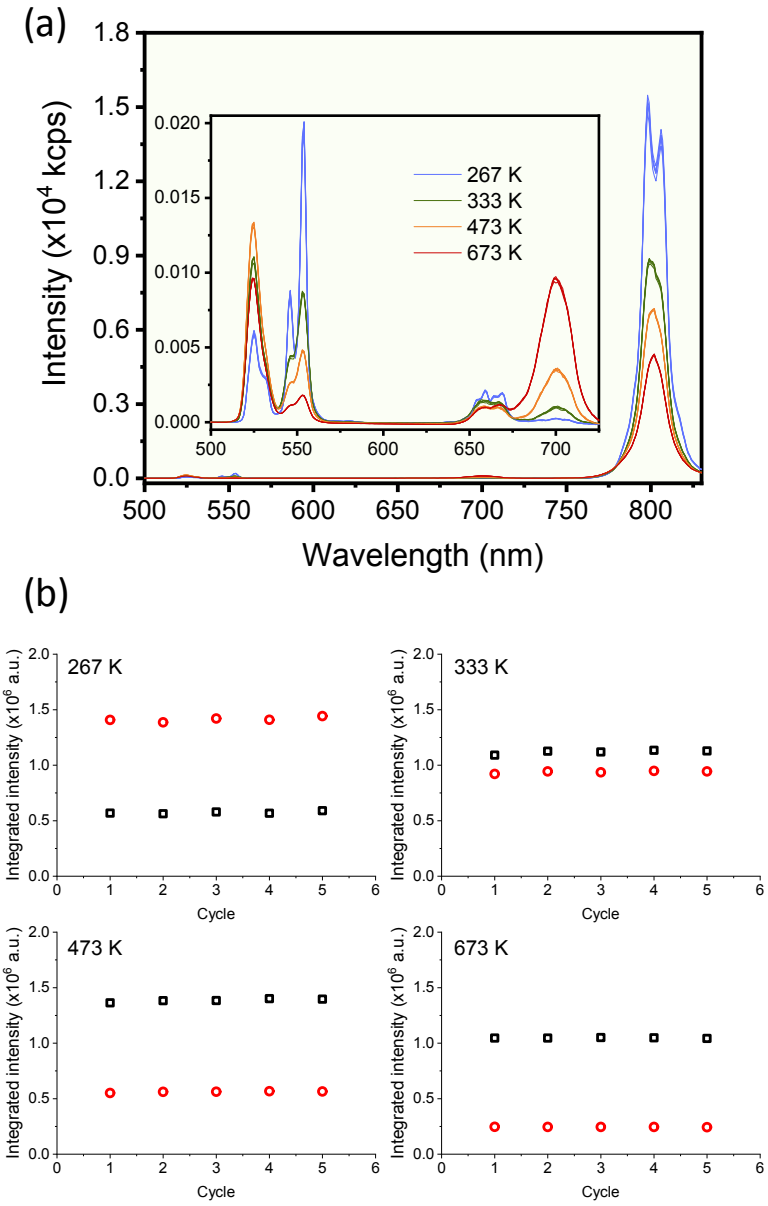

Figure S20. (a) Upconversion spectra (λ_{exc}=980 nm, P = 34.8 W cm^{-2}) at different temperatures demonstrating the reproducibility of $Y_{0.77}Yb_{0.20}Tm_{0.02}Er_{0.01}VO_4$ particles upon five heating-cooling cycles (267-673 K). (b) Integrated intensities of the $^2H_{11/2}\rightarrow{}^4I_{15/2}$ ($I_{525\ nm}$, black squares) and $^4S_{3/2}\rightarrow{}^4I_{15/2}$ ($I_{553\ nm}$, red squares) Er^{3+} transitions at different temperatures.

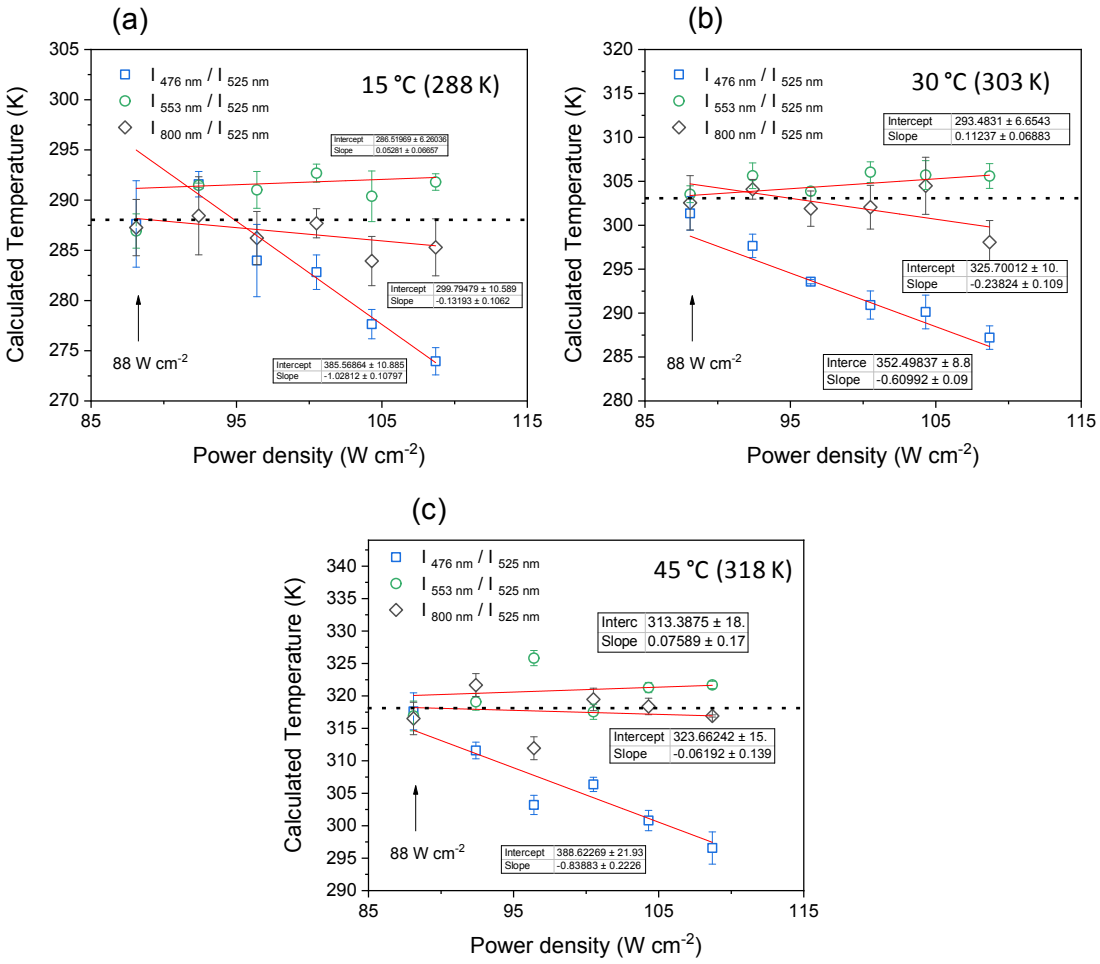

Figure S21. Dependence of calculated temperature (using the thermometric calibration) against the excitation power for $Y_{0.77}Yb_{0.20}Tm_{0.02}Er_{0.01}VO_4$ colloidal particles under NIR excitation (λ_{exc}=980 nm) at temperatures set at (a) 15 °C (288 K), (b) 30 °C (303 K), and (c) 45 °C (318 K) [excitation power used for thermometric calibration was 88 W cm^{-2}] for the $I_{476\ nm}/I_{525\ nm}$ (blue squares), $I_{553\ nm}/I_{525\ nm}$ (green circles), and $I_{801\ nm}/I_{525\ nm}$ (black diamonds) ratios. Insets show intercepts and slopes for linear fits (red lines) calculated for the three intensity ratios in each case.

References

1. C. D. S. Brites, A. Millán and L. D. Carlos, in *Handbook on the Physics and Chemistry of Rare Earths*, ed. J.-C. G. Bünzli and V. K. Pecharsky, Elsevier, Amsterdam, 1st edn., 2016, vol. 49, ch. 281, 339-427.
2. J. Rocha, C. D. S. Brites and L. D. Carlos, *Chem. Eur. J.*, 2016, **22**, 14782.
3. N. F. Mott, *Proc. R. Soc.*, 1938, **167**, 384.
4. F. Seitz, *Trans. Faraday Soc.*, 1939,**35**, 74.
5. P. C. de Sousa Filho, J. Alain, G. Leménager, E. Larquet, J. Fick, O. A. Serra and T. Gacoin, *J. Phys. Chem. C*, 2019, **123**, 2441.